Proceedings of the Royal Society A, 469 (2013), 20120458

Effect of Aluminium on Hydrogen-induced Fracture Behaviour in Austenitic Fe–Mn–C Steel

Joo Hyun Ryu[1], Sung Kyu Kim[2], Chong Soo Lee[1], Dong–Woo Suh[1] and H. K. D. H. Bhadeshia[1,3]

[1]Graduate Institute of Ferrous Technology (GIFT)
Pohang University of Science and Technology (POSTECH)
Pohang 790-784, Republic of Korea

[2]POSCO
Technical research laboratory, Kwangyang, Republic of Korea

[3]University of Cambridge
Materials Science and Metallurgy, Cambridge CB2 3QZ, U.K.

abstract

It is known empirically that the addition of aluminium as a solute in high–Mn austenitic steels dramatically improves their resistance to hydrogen–induced embrittlement. A variety of experimental techniques including the characterisation of trapping sites and high–resolution observation of fracture facets, have been used to reveal the mechanism by which aluminium induces this effect. It is found that transgranular fracture is promoted by the segregation of hydrogen to mechanical twin interfaces and to any ϵ–martensite that is induced during deformation. Since aluminium increases the stacking fault energy of austenite, the tendency for mechanical twinning is reduced, and the formation of deformation–induced martensite eliminated. These two effects contribute to the resistance of the aluminium–alloyed steel to hydrogen embrittlement.

1. Introduction

Austenitic Fe-Mn-C alloys have interesting combinations of strength and ductility (De Cooman et al., 2011; Frommeyer et al., 2003), although these are yet to be implemented on a large scale. Some of the initial momentum towards exploitation in the automotive industry was jeopardised by reports of delayed fracture in formed components, an effect often attributed to hydrogen (Chin et al., 2011; Kim et al., 2008). Given that austenitic steels do not generally suffer from hydrogen embrittlement (Jung et al., 2008; Mittal et al., 1994; Ronevich et al., 2010; So et al., 2009), one interpretation is that the formation of α' martensite during

Proc. R. Soc. A 1–22; doi: 10.1098/rspa.00000000

forming operations is necessary for the onset of delayed fracture in Fe-16Mn-0.6C wt% (Kim et al., 2008).

However, an alloy much more resistant to martensitic transformation, with composition Fe-22Mn-0.6C wt% also exhibited static fracture after cup-forming and exposure to air for 7 days; in this case the failure was attributed to localised deformation and twinning (Chin et al., 2011).

Aluminium additions to such alloys are known to enhance the resistance to static failure; it is speculated that aluminium promotes more homogeneous deformation via its influence on the increase of the stacking fault energy (Dumay et al., 2008; Kim et al., 2011). Alloying with aluminium has been shown to lead to a reduction of residual stress in Fe-18Mn-0.6C wt% and this could contribute to an increased resistance to hydrogen embrittlement (Chun et al., 2012b). The formation of an alumina layer on the surface of the steel during hydrogen charging of a Fe-19Mn-0.6C-2Al wt% steel may hinder hydrogen absorption on the surface (Park et al., 2012).

The actual mechanism by which the dissolved aluminium enhances the resistance to delayed fracture therefore remains uncertain, and the specific role of hydrogen needs clarification. The present work is an attempt to clarify the role of aluminium on hydrogen-induced fracture in austenitic Fe-Mn-C steels using slow strain rate tensile tests with *in-situ* hydrogen charging and a variety of high–resolution characterisation techniques.

2. Experimental Details

Alloys

Table 1 lists the chemical compositions of two Fe-0.6C-18Mn wt% based alloys, one without aluminium and the other containing 1.5 wt% Al in solution. The oxygen content is 45 and 21 ppm, respectively. Vacuum induction–melted ingots of dimensions $300 \times 150 \times 100$ mm were heated at 1150 °C for 2 h and hot–rolled to 3 mm in thickness with a finishing temperature above 900 °C followed by air cooling to room temperature. The alloys were cold–rolled to 1.2 mm in thickness after pickling in a 10 % HCl solution and then intercritically annealed using an infrared furnace at 900 °C for 15 min. The heating and cooling rates were $\pm 10\,^{\circ}\mathrm{C\,s^{-1}}$ respectively.

Microstructural characterisation

For microstructural characterisation, the samples were mechanically ground and polished. The microstructures were observed using a field emission scanning electron microscope (FE-SEM) equipped with an electron back-scattered diffraction (EBSD) facility. The step size for EBSD measurement was 0.1 µm. The constituent phases were determined using X-ray diffraction (XRD) with Cu K_α

radiation. Integrated intensities of $10\bar{1}0_\epsilon$, $10\bar{1}1_\epsilon$, $10\bar{1}2_\epsilon$, $10\bar{1}3_\epsilon$ and 111_γ, 200_γ, 220_γ reflections were used for the quantitative analysis of phase fractions (Yang and Luo, 2000). A focused ion beam was used in preparing specimens for transmission electron microscopy to investigate the microstructure around the fracture surfaces which were protected with carbon and platinum deposition.

Hydrogen charging and thermal desorption spectroscopy

Tensile test coupons with a 50 mm gauge length, 12.5 mm width and 1.2 mm thickness were prepared according to the ASTM E8M standard, polished with the 800 SiC grit papers and charged electrochemically with the hydrogen in an aqueous mixture of 3% NaCl + 0.3 NH_4SCN at 0.5–5 A m^{-2}. Thermal desorption spectroscopy (TDS) with gas chromatography was conducted at a constant heating rate of 100 °C h^{-1} to a maximum temperature of 300 °C. The gauge length part of each charged tensile sample was cut immediately after charging and placed in the TDS furnace. The sample gas was analysed at 3 min intervals using helium as a carrier gas and the desorption rate was defined as the amount of hydrogen evolved in 1 min per gram of the specimen. A standard mixture He + 10.2 volume ppm of H_2 was used for the calibration.

Hydrogen microprinting technique

Hydrogen emission from samples was visualised using the hydrogen microprint technique (HMT) (Matsunaga and Noda, 2011; Ovejero-garcia, 1985). The samples were mechanically polished and then charged with hydrogen. Then, the sample surface was covered with a mixture of 5 g gelatin-based AgBr emulsion (Ilford L-4) + 10 ml distilled water. After holding the sample in ambient air for 10 min, it was dipped into 38 % formalin for 1 s to harden the gelatin film, and then immersed in 17 % $Na_2S_2O_3$ + 5 % $NaNO_2$ aqueous solution for 3 min to wash away any unreacted AgBr particles. After rinsing the sample surface with distilled water and drying, silver particles present on the sample surface were observed.

Mechanical tests

Slow strain rate tensile (SSRT) tests were conducted at a constant crosshead speed of 0.03 mm min^{-1}, corresponding to a nominal strain rate of 10^{-5} s^{-1}, with *in-situ* hydrogen charging. For tensile specimens with a gauge length of 50 mm, which were pre-charged with hydrogen to examine the hydrogen-induced martensite transformation in the course of deformation, a faster strain rate of 10^{-3} s^{-1} was used to minimise the loss of hydrogen during test. The detailed experimental sets have been described elsewhere (Ryu, 2012).

3. Results and Discussion

Microstructure and tensile properties without hydrogen

Figs. 1 (a) and (b) show representative microstructures of the 0Al and 1.5Al alloys in the annealed condition, with grain sizes measured as mean lineal intercepts (Dehoff and Rhines, 1968) of 5.2±0.6 and 6±0.3 µm respectively; the measurements include annealing–twin boundaries. The stress-strain curves of uncharged samples are presented in Fig. 2. The large degree of strain hardening is a consequence of both dynamic strain aging (Adler et al., 1986; Shun et al., 1992) and the fact that the effective grain size is progressively reduced by the partitioning of the austenite grains due to mechanical twinning during the course of deformation (Allain et al., 2004; Bouaziz et al., 2011; Idrissi et al., 2010). The addition of Al decreases the rate of hardening because it reduces the strain aging that leads to serrated flow curves, and also the tendency to mechanical twin formation by increasing the stacking fault energy of the austenite (Jeong et al., 2012; Kim et al., 2011). Figures 1 (c) and (d) show the microstructure of the samples strained to 30% elongation. As expected, a relatively large quantity of mechanical twinning has occurred in the 0Al alloy. The X–ray diffraction profiles of 0Al alloy in Fig. 3 confirm that within the limits of detection, deformation-induced martensitic transformation does not occur in the fractured tensile specimens including the necked region. The same result was observed in 1.5Al the alloy, which is consistent with previous reports (Chun et al., 2012b; Jeong et al., 2012; Jung et al., 2008).

Fracture behaviour during hydrogen charging

The stress-strain curves from the slow strain-rate tests where hydrogen was charged during the tensile testing using current densities of 0.5, 1 and 5 $A\,m^{-2}$, are given in Fig. 2. For both alloys, the work hardening behaviour was hardly affected by hydrogen charging, but the total elongation was significantly reduced as the charging current increased (Koyama et al., 2011). The degradation of mechanical properties is quantified in Fig. 4 which illustrates the loss of ultimate tensile strength and elongation as follows:

$$\mathrm{El}_{\mathrm{loss}} = \frac{\mathrm{El}_{\mathrm{uncharged}} - \mathrm{El}_{\mathrm{charged}}}{\mathrm{El}_{\mathrm{uncharged}}} \times 100 \tag{3.1}$$

$$\mathrm{UTS}_{\mathrm{loss}} = \frac{\mathrm{UTS}_{\mathrm{uncharged}} - \mathrm{UTS}_{\mathrm{charged}}}{\mathrm{UTS}_{\mathrm{uncharged}}} \times 100 \tag{3.2}$$

Fig. 4 indicates that the extent of deterioration in mechanical properties increases with the hydrogen–charging current density, and that the addition of aluminium mitigates the loss in properties. The mechanism of fracture is not uniform across the cross section of the tensile samples, with the regions near the surface failing in a brittle manner, Fig. 5. In contrast, the central regions of the tensile specimens failed in a ductile manner, with dimples characteristic of

plasticity due to void nucleation and coalescence. Since the depth of the brittle zone increased as a function of the current density, it appears that brittle failure occurs at the surface region having more concentration of hydrogen due to its in-situ charging during the test.

The relatively small brittle zones observed in the 1.5Al alloy are consistent with the fact that its mechanical properties are less sensitive to hydrogen. To identify the role of aluminium in relation to hydrogen, thermal desorption spectroscopy (TDS) analysis was performed on the fractured samples. Fig. 6 shows the TDS profiles and the results are summarised in Table 2. The quantity of hydrogen in the 1.5Al alloy is in fact found to be larger than in the 0Al alloy, so its enhanced resistance to hydrogen embrittlement cannot be explained in terms of the hydrogen concentration. It is possible therefore that the shallow penetration of hydrogen in the aluminium–containing alloy is due to other effects related to the defects created during deformation, and the associated trapping of hydrogen. The fact that the fracture surfaces illustrated in Fig. 7 show both transgranular (B) as well as intergranular (A) brittle–fracture, indicates that hydrogen trapping inside of the austenite grain is no less important than that at grain boundaries in understanding the mechanical degradation. Indeed, given the reasonably large grain size and hence small grain surface per unit volume, it is likely that trapping within austenite grains is a key factor in explaining the differences between the aluminium–containing and aluminium–free alloys.

Trapping of hydrogen

The TDS profiles in Fig. 6 show that much of the hydrogen charged into the samples is released below 200 °C, implying that it is reversibly–trapped, diffusible hydrogen. The possible trapping sites are likely to be grain boundaries or dislocations within the austenite. Figure 8 (a) shows the change in diffusible hydrogen content as a function of the austenite grain size (mean lineal intercept L), where the latter was controlled by adjusting the annealing temperature. The increase in the hydrogen content with greater grain boundary area per unit volume, $2L^{-1}$, for identical charging conditions (1 A m^2 for 72 h), suggests that the boundaries contribute as trapping sites. Similar results are shown in Fig. 8 (b) indicating that the hydrogen content gradually increases with the pre-strain of 15, 30 and 45 % followed by hydrogen charging at 1 A m^2 for 72 h; here the pre-strain is implied to lead to an increase in the dislocation density before hydrogen charging. To establish the role of dislocations, samples pre-strained to 30% elongation were annealed to induce recovery without changing the austenite grain size, at 550°C for 10 min (Kang et al., 2010), and then subjected to hydrogen charging. It is clear that the amount of reversibly–trapped diffusible hydrogen is reduced, thus demonstrating the role of dislocations as trapping sites.

In austenitic Fe-Mn-C steels of the type considered here, deformation is known to generate mechanical twins (Frommeyer et al., 2003), which naturally may participate in hydrogen trapping. So et al. (So et al., 2009) reported that mechanical twin boundaries are strong traps with a binding energy evaluated to be 62 kJ mol^{-1}. In their analysis using the Kissinger equation (Kissinger, 1957),

a separate TDS peak over the range 200–300 °C was attributed to mechanical twinning, but such a peak was not observed in the present work even in the samples strained to 45%. To reveal the hydrogen trapping behaviour at twins by direct observation, a hydrogen microprinting technique (HMT) was employed. Figures 9 (a) and (c) show the microprint images from the sample strained to 30% followed by hydrogen charging at $1\,\mathrm{A\,m^{-2}}$ for 72 h. The silver particles precipitate at locations rich in hydrogen. A comparison of the microprint image with a corresponding crystallographic orientation map in Fig. 9 (d) using EBSD after removing the silver particles by slight polishing confirmed the segregation of hydrogen in the mechanical twins.

It is particularly noteworthy that silver particles hardly deposited on the sample subjected to hydrogen charging followed by heating up to 200 °C, Figs. 9 (b). It appears that mechanical twins, like grain boundaries and dislocations, yield any trapped hydrogen during heating below 200 °C, and therefore are not to be regarded as particularly strong traps for hydrogen. Indeed, Idrissi et al. (Idrissi et al., 2010) reported that the mechanical twins contain a huge density of dislocations resulting from the mechanism of twin nucleation and growth. Therefore, any trapping associated with the twins may in fact be due largely to their dislocation content.

Hydrogen-induced transgranular fracture

The desorption spectroscopy data combined with the microprinting images confirms that the diffusible hydrogen was trapped at grain boundaries and mechanical twins. Hydrogen transported by dislocation gliding towards and across grain and twin interfaces during deformation (Louthan et al., 1972; Tien et al., 1976) will tend to accumulate at and embrittle those interfaces leading to either intergranular separation at grain boundaries, or transgranular fracture associated with the twin interfaces. It is noted that these interfaces are also associated with numerous dislocations which play a role as trapping site of hydrogen. If this interpretation is correct, then the addition of aluminium to austenitic Fe-Mn-C will have a beneficial effect on toughness via the suppression of crack initiation within the austenite grains, given that the aluminium reduces the probability of mechanical twinning (Jeong et al., 2012).

However, there may also be a role of ϵ–martensite, which could be detected from the X–ray diffraction profiles of the 0Al alloy fractured in slow strain–rate tensile tests conducted during hydrogen charging as shown in Fig. 10 (a), which is different from the result of deformation without hydrogen in Fig 3. The fraction of ϵ–martensite was evaluated to be 0.11 ± 0.02, but this represents the quantity in the surface layer penetrated by the X–rays, a layer which also contains the largest quantity of hydrogen given its low diffusivity in austenite. For detailed examination, the samples pre-charged at $1\,\mathrm{A\ m^{-2}}$ for 72 h were deformed at a higher strain rate of $10^{-3}\ \mathrm{s^{-1}}$ to minimise the loss of hydrogen during the test. The total amount of diffusible hydrogen before tensile testing was evaluated to be 0.36 and 0.48 ppmw for the 0Al and 1.5Al alloys, respectively. The diffraction profiles presented in Fig. 10 (b) indicate that ϵ–martensite formed in the 0Al

alloy strained to 5 and 30%. The fraction of ϵ–martensite in the surface layer increases with amount of deformation to 0.05±0.02 to 0.09±0.02 respectively. Since the ϵ–martensite was not detected in the unstrained condition even with the addition of hydrogen, it is believed to be induced by deformation. The martensite was not observed in the 1.5Al alloy even though it contains a greater hydrogen content than the 0Al alloy. The susceptibility to transformation in the 0Al alloy is probably related with the reduction in stacking fault energy (SFE) when the steel is charged with hydrogen. Whiteman and Troiano (Whiteman and Troiano, 1964) reported such a decrease in the SFE caused by hydrogen on the basis of transmission electron microscopy observations of 310 stainless steel. Pontini and Hermida (Pontini and Hermida, 1997) found a reduction of 37 % in the SFE at room temperature in 304 stainless steel containing 274 ppmw hydrogen. One mechanism for these observations is the reduction in energy associated with the formation of H-H pairs during faulting (Hermida and Roviglione, 1998; Moro et al., 1998). It is also known that when the stacking fault energy is reduced to less than $\approx 16\,\mathrm{mJ\,m^{-2}}$, there is a tendency to form ϵ–martensite instead of mechanical twinning during deformation (Frommeyer et al., 2003). Since the reported SFEs for 0Al and 1.5Al are 19 and $28\,\mathrm{mJ\,m^{-2}}$ respectively (Jeong et al., 2012), any reduction in SFE for the hydrogen–containing 0Al alloy will make it susceptible to the formation of ϵ–martensite during deformation; this is unlikely for the aluminium–rich steel where the fault energy is much greater.

Several investigators have to date reported hydrogen-induced ϵ– martensite when large concentrations are introduced into undeformed, relatively unstable 304 stainless steel (Yang and Luo, 2000), and in the more stable 310 stainless steel (Minkovitz and Eliezer, 1982; Narita et al., 1982). Some cracks were found to initiate and propagate through the ϵ–martensite or along ϵ/γ interfaces in these alloys. Recently, Chun et al. (Chun et al., 2012a) investigated the effect of ϵ–martensite on the hydrogen degradation behaviour of a Fe-15Mn-2Cr-0.6C (wt %) alloy, concluding that the embrittlement is worse when the fraction of ϵ–martensite in the initial microstructure is large. Fig. 11 shows the EBSD mapping of sample surfaces subjected to charging at $1\,\mathrm{A\,m^{-2}}$ for 72 h followed by straining in tension to 30%. The formation of ϵ–martensite is seen clearly in the 0Al alloy but not in the aluminium-rich variant. Interestingly, some of the transgranular cracks are located adjacent to the ϵ–martensite as indicated by arrows, which implies it is a crack initiation site for transgranular fracture of the type illustrated in Fig. 7. On the other hand, the microstructure free from the ϵ–martensite in the 1.5Al alloy does not suffer from transgranular cracks.

The influence of ϵ–martensite was examined by preparing samples for transmission electron microscopy using the focused ion–beam method, such that they contain the transgranular fracture surfaces generated during the slow strain–rate test of the 0Al alloy using in-situ hydrogen charging. Figures 12 (a) and (b) show vividly that the transgranular fracture surface is parallel to the interface between ϵ–martensite and austenite, indicating this kind of fracture is likely to occur along the ϵ/γ interfaces. A similar characterisation for 1.5Al alloy is shown in Fig. 13, and reveals that the transgranular fracture surface is parallel to the mechanical twin interfaces, an observation recently confirmed by Koyama et al. (Koyama et al., 2012) using electron channeling contrast images. These results

indicate that in the presence of hydrogen, the formation of mechanical twinning as well as ϵ–martensite provides sites which are vulnerable to cracking during deformation. Therefore, aluminium helps prevent mechanical degradation due to hydrogen by suppressing the generation not only of ϵ–martensite but also the mechanical twinning.

4. Conclusions

The mechanical degradation by hydrogen in austenitic Fe-Mn-C and Fe-Mn-C-Al steels has been characterised using tensile tests conducted during hydrogen charging. The following conclusions can be reached on the basis of a variety of observations:

1. The surface layers of the test specimens, containing the largest concentrations of hydrogen, tend to undergo brittle fracture in both the intergranular and transgranular modes due to the preferential location of hydrogen at interfaces. The thickness of brittle fractured zone is less than a few hundred micrometer. Transgranular fracture is promoted when the density of twin interfaces is large, whereas grain boundary separation occurs when mechanical twinning is suppressed. The modes here refer to fracture relative to the austenite grain boundaries.

2. If the steel is relatively unstable then the introduction of hydrogen in combination with plastic strain leads to deformation-induced ϵ–martensite which is particularly susceptible to hydrogen embrittlement and leads to transgranular cracking parallel to the ϵ/γ interfaces.

3. The role of aluminium as a solute in the high-manganese austenitic steels is two fold. It increases the stacking fault energy of the steel and hence reduces the probability of mechanical twinning during deformation. The higher stacking fault energy at the same time eliminates the formation of ϵ–martensite. Both of these effects lead to a greater resistance of the steel to hydrogen embrittlement.

Acknowledgments: This research was supported by WCU (World Class University) programme through the National Research Foundation of Korea funded by the Ministry of Education, Science and Technology (R32-10147).

References

Adler, P. H., Olson, G. B., Owen, W. S., 1986. Strain hardening of hadfield manganese steel. Metall Trans A 17, 1725–1737.

Allain, S., Chateau, J., Bouaziz, O., Migot, S., Guelton, N., 2004. Correlations between the calculated stacking fault energy and the plasticity mechanisms in Fe–Mn–C alloys. Mater Sci Eng A 387, 158–162.

Bouaziz, O., Allain, S., Scott, C. P., Cugy, P., Barbier, D., 2011. High manganese austenitic twinning induced plasticity steels: A review of the microstructure properties relationships. Curr Opin Solid St M 15, 141–168.

Chin, K. G., Kang, C. Y., Shin, S. Y., Hong, S. K., Lee, S. H., Kim, H. S., Kim, K. H., Kim, N. J., 2011. Effects of Al addition on deformation and fracture mechanisms in two high manganese twip steels. Mater Sci Eng A 528, 2922–2928.

Chun, Y., Kim, J. S., Park, K. T., Lee, Y. K., Lee, C. S., 2012a. Role of epsilon martensite in tensile properties and hydrogen degradation of high-Mn steels. Mater Sci Eng A 533, 87–95.

Chun, Y. S., Park, K. T., Lee, C. S., 2012b. Delayed static failure of twinning-induced plasticity steels. Scripta Mater 66, 960–965.

De Cooman, B., Chin, K., Kim, J., 2011. New Trends and Developments in Automotive System Engineering. Rijeka(Croatia): InTech, Ch. High Mn TWIP Steels for Automotive Applications, Ed. by M. Chiaberge, pp. 101–128.

Dehoff, R., Rhines, F., 1968. Quantitative Microscopy. McGraw Hill, New York.

Dumay, A., Chateau, J. P., Allain, S., Migot, S., Bouaziz, O., 2008. Influence of addition elements on the stacking-fault energy and mechanical properties of an austenitic Fe–Mn–C steel. Mater Sci Eng A 483-484, 184–187.

Frommeyer, G., Brux, U., Neumann, P., 2003. Supra-ductile anf high-strength manganese-TRIP/TWIP steels for high energy absorption purpose. ISIJ Int 43, 438–446.

Hermida, J. D., Roviglione, A., 1998. Stacking fault energy decrease in austenitic stainless steel induced by hydrogen pairs formation. Scripta Mater 39, 1145–1149.

Idrissi, H., Renard, K., Schryversa, D., Jacques, P. J., 2010. On the relationship between the twin internal structure and the work-hardening rate of TWIP steels. Scripta Mater 63, 961–964.

Jeong, J. S., Woo, W., Oh, K. H., Kwon, S. K., Koo, Y. M., 2012. In situ neutron diffraction study of the microstructure and tensile deformation behavior in Al-added high manganese austenitic steels. Acta Mater 60, 2290–2299.

Jung, J. K., Lee, O. Y., Park, Y. K., Kim, D. E., G., C. K., 2008. Hydrogen embrittlement behavior of high Mn TRIP/TWIP steels. Korean J Mater Res 18, 394–399.

Kang, S. G., Jung, Y. S., Jun, J. H., Lee, Y. K., 2010. Effects of recrystallization annealing temperature on carbide precipitation, microstructure, and mechanical properties in Fe–18Mn-0.6C-1.5Al TWIP steel. Mater Sci Eng A 527, 745–751.

Kim, J. K., Lee, S. J., De Cooman, B. C., 2011. Effect of Al on the stacking fault energy of Fe-18Mn-0.6C twinning-induced plasticity. Scripta Mater 65, 363–366.

Kim, Y., Kang, N., Park, Y., Choi, I., Kim, G., Kim, S., Cho, K., 2008. Effects of the strain induced martensite transformation on the delayed fracture for Al-added TWIP steel. J Korean Inst Met Mater 46, 780–787.

Kissinger, H. E., 1957. Reaction kinetics in differential thermal analysis. Anal Chem 29, 1702–1706.

Koyama, M., Akiyama, E., Sawaguchi, T., Raabe, D., Tsuzaki, K., 2012. Hydrogen-induced cracking at grain and twin boundaries in an Fe-Mn-C austenitic steel. Scripta Mater 66, 459–462.

Koyama, M., Akiyama, E., Tsuzaki, K., 2011. Hydrogen embrittlement in a Fe–Mn–C ternary twinning-induced plasticity steel. Corros Sci 54, 1–4.

Louthan, M. R., Caskey, G. R., Donovan, J. A., Rawl, D. E., 1972. Hydrogen embrittlement of metals. Mater Sci Eng 10, 357–368.

Matsunaga, H., Noda, H., 2011. Visualization of hydrogen diffusion in a hydrogen-enhanced fatigue crack growth in type 304 stainless steel. Metall Mater Trans A 42, 2696–2705.

Minkovitz, E., Eliezer, E., 1982. Phase transitions at the crack tip in type 316l stainless steel cathodically hydrogen charged. Scripta Metall Mater 16, 981–984.

Mittal, S. C., Prasad, R. C., Deshmuk, M. B., 1994. Effect of hydrogen on fracture of austenitic Fe–Mn–Al steel. ISIJ Int 34, 211–216.

Moro, L., Obiol, E., Roviglione, A., Hermida, J. D., A, J., 1998. A theory of hydrogen trapping in a faulted zone of fcc iron. J Phys D Appl Phys 31, 893–899.

Narita, N., Altstetter, C. J., Birnbaum, H. K., 1982. Hydrogen-related phase transformations in austenitic stainless steels. Metall Trans A 13, 1355–1365.

Ovejero-garcia, J., 1985. Hydrogen microprint technique in the study of hydrogen in steels. J Mater Sci 20, 2623–2629.

Park, I., Jeong, K., Jung, J., Lee, C. S., Lee, Y., 2012. The mechanism of enhanced resistance to the hydrogen delayed fracture in Al-added Fe-18Mn-0.6C twinning-induced plasticity steels. Int J Hydrogen Energ 37, 9925–9932.

Pontini, A. E., Hermida, J. D., 1997. X-ray diffraction measurement of the stacking fault energy reduction induced by hydrogen in an AISI 304 steel. Scripta Mater 37, 1831–1837.

Ronevich, J. A., Speer, J. G., Matlock, D. K., 2010. Hydrogen Embrittlement of Commercially Produced Advanced High Strength Sheet Steels. SAE International Journal of Materials and Manufacturing 3, 255–267.

Ryu, J. H., 2012. Hydrogen embrittlement in TRIP and TWIP steels. Ph.D. Thesis, Republic of Korea: POSTECH.

Shun, T. S., Wan, C. M., Byrne, J. G., 1992. A study of work hardening in austenitic Fe–Mn-C and Fe-Mn-Al-C alloys. Acta Metall Mater 40, 3407–3412.

So, K. H., Kim, J. S., Chun, Y. S., Park, K. T., Lee, Y. G., Lee, C. S., 2009. Effect of hydrogenon fracture of austenitic Fe-Mn-Al steel. ISIJ Int 49, 1952–1959.

Tien, J. K., Thompson, A. W., Bernstein, I. M., Richards, R. J., 1976. Hydrogen transport by dislocations. Metall Trans A 7, 821–829.

Whiteman, M. B., Troiano, A. R., 1964. The influence of hydrogen on the stacking fault energy of an austenitic stainless steel. Phys Status Solidi 7, 109–110.

Yang, Q., Luo, J. L., 2000. Martensite transformation and surface cracking of hydrogen charged and outgassed type 304 stainless steel. Mater Sci Eng A 288, 75–83.

Table 1. Chemical compositions (wt%) of alloys

	C	Mn	Al
0Al	0.6	18	0
1.5Al	0.6	18	1.49

Table 2. Hygrogen content C^H of fractured sample under in-situ charging at various current density

	Current density / A m^{-2}	C^H / ppmw	Charging time /s
0Al	0.5	0.31	42132
	1	0.28	36117
	5	0.21	26985
1.5Al	0.5	0.53	49545
	1	0.48	45726
	5	0.45	32720

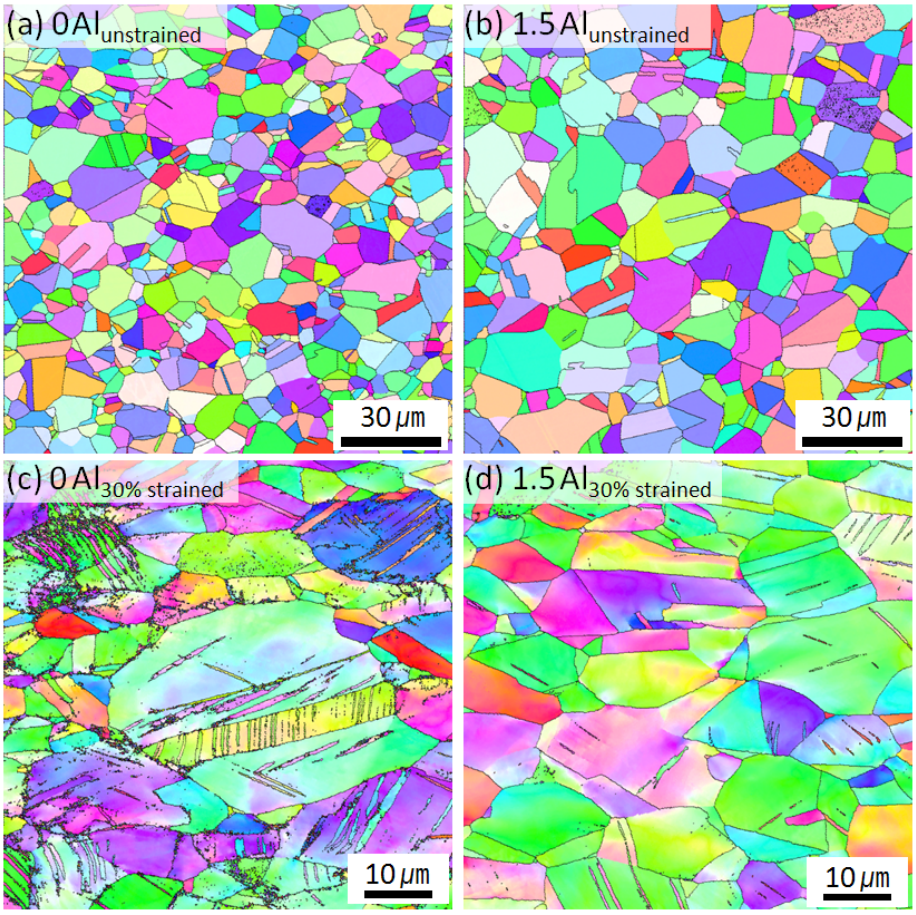

Figure 1. EBSD mapping of alloys after annealing at 900 °C for 15 min. (a) 0Al, (b) 1.5Al alloys are unstrained and (c) 0Al, (d) 1.5Al are strained to 30%. None of these samples were charged with hydrogen.

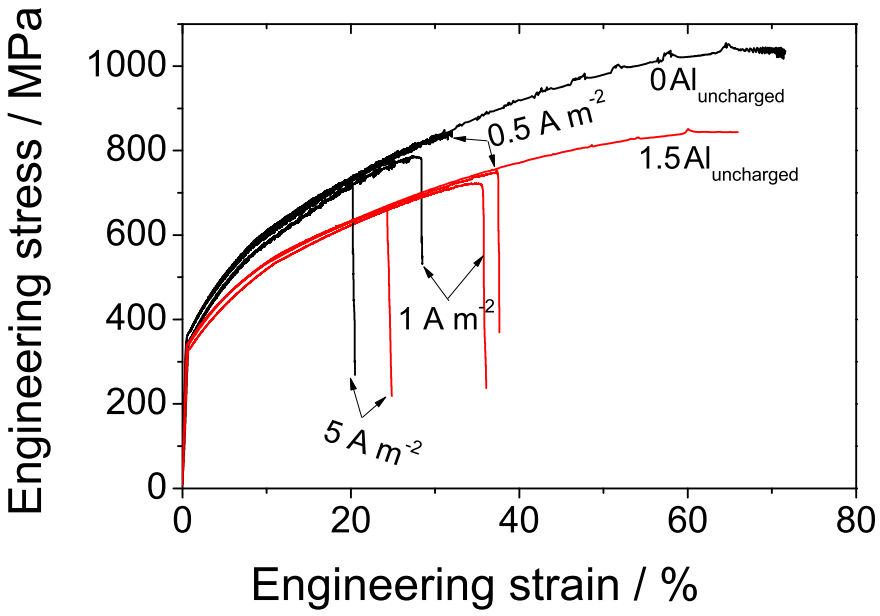

Figure 2. Stress-strain curves of as-annealed 0Al and 1.5Al alloys compared with those under in-situ hydrogen charging at various current densities

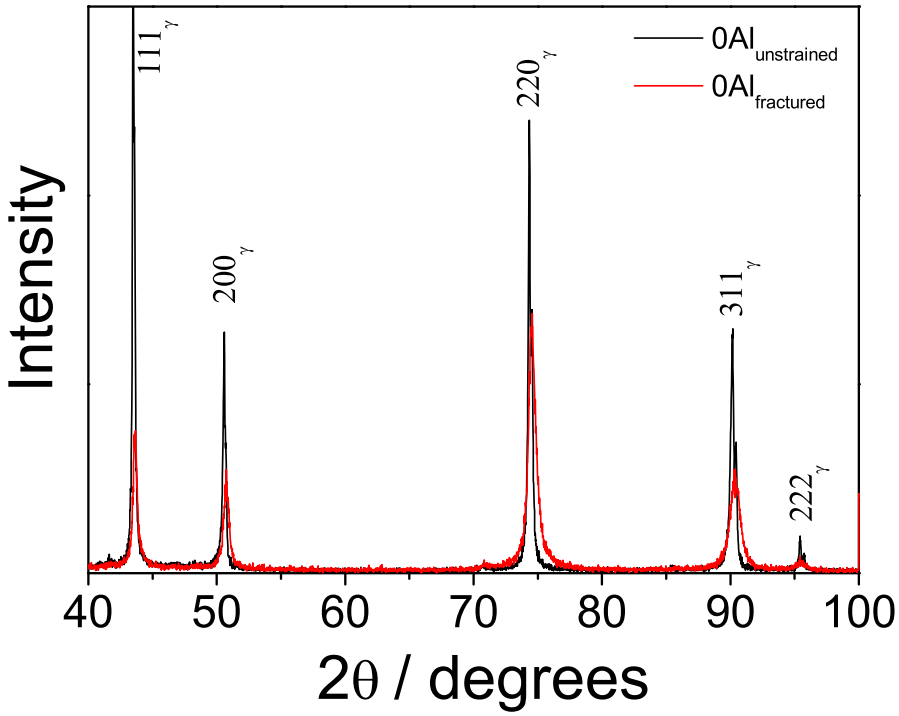

Figure 3. XRD profiles from as-annealed and fractured 0Al alloy without hydrogen charging

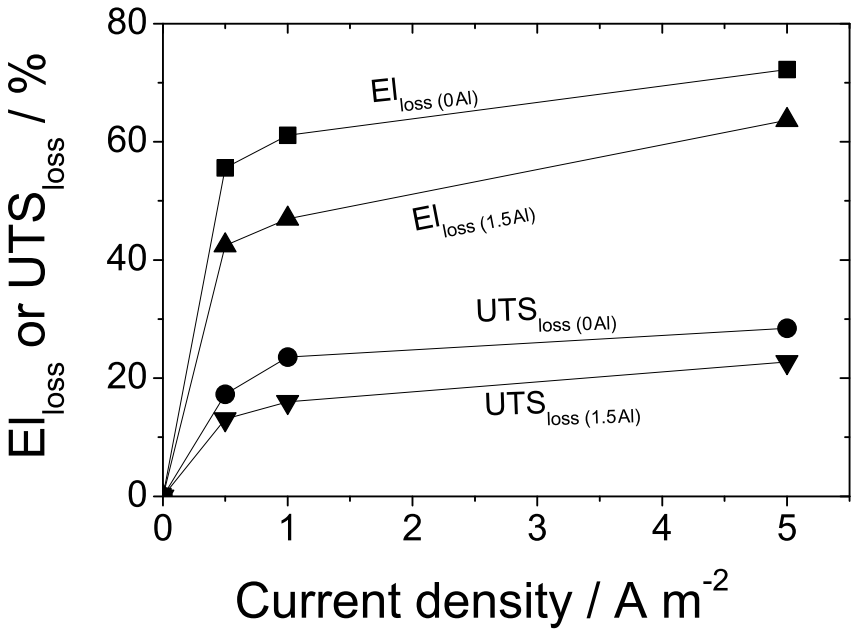

Figure 4. Loss of ultimate tensile strength and elongation by hydrogen as a function of current density

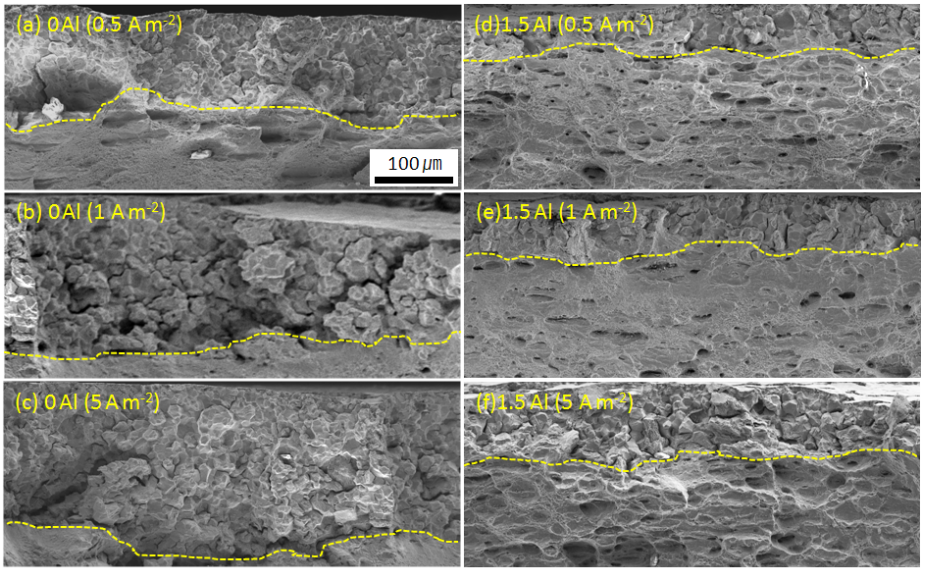

Figure 5. Fractography beneath the specimen surface in 0Al and 1.5Al alloys charged with various current densities. Broken lines indicate the boundaries of brittle fractured layers.

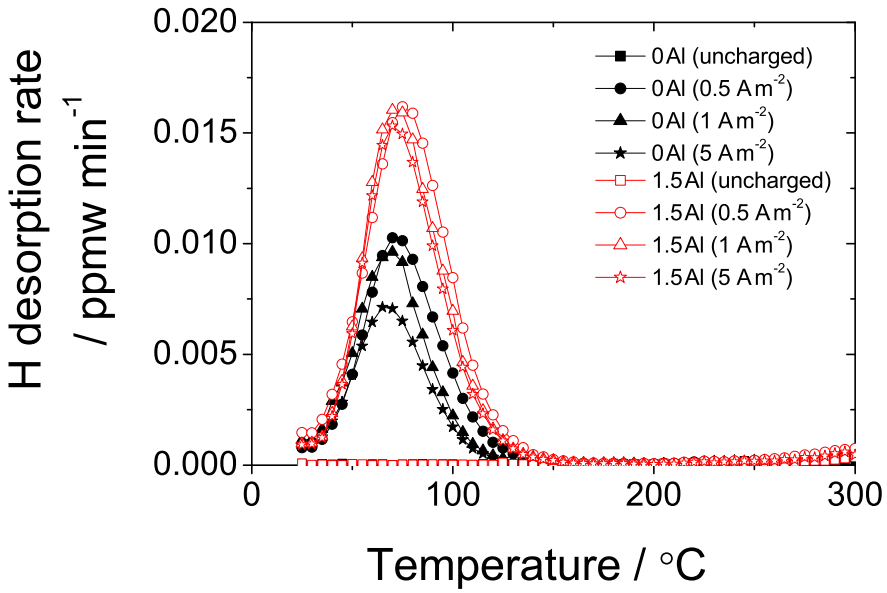

Figure 6. Thermal desorption profiles from the fractured samples in SSRT test under in-site hydrogen charging. Note that the smaller quantity of hydrogen at higher current densities is because of the shorter charging time due to earlier failure of tensile specimen 2.

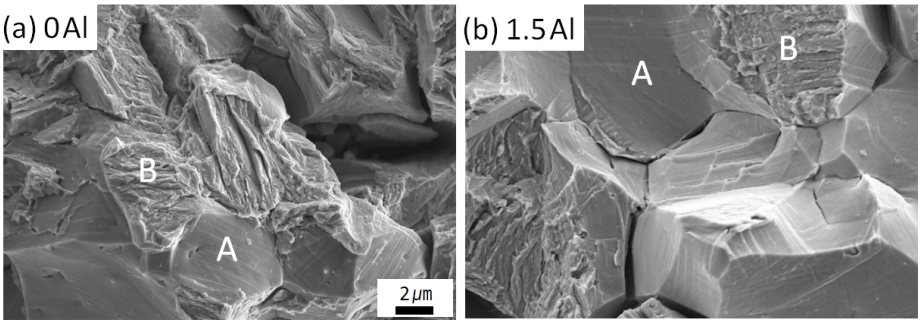

Figure 7. Fracture surface in the brittle fractured layer showing both intergranular (A) and transgranular (B) fractures in samples charged with 1 A m^{-2}

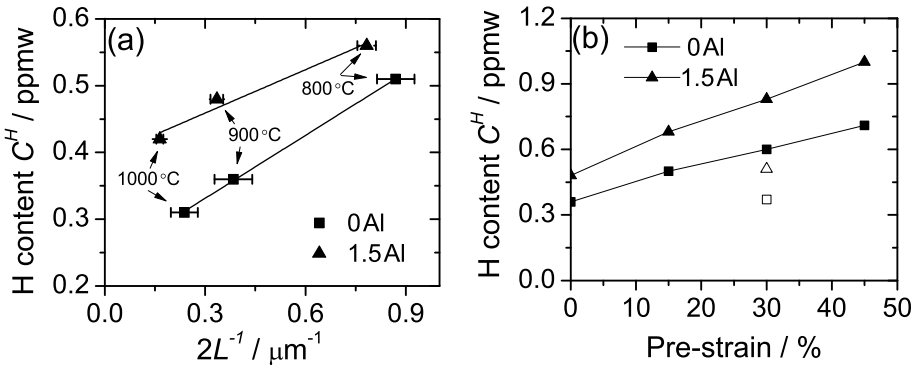

Figure 8. Total diffusible hydrogen content in specimens charged at 1 A m^{-2} for 72 h as a function of (a) grain boundary area per unit volume and (b) amount of pre-strain. The open symbols in (b) represent for the sample subjected to pre-strain, annealing at 550°C, followed by hydrogen charging.

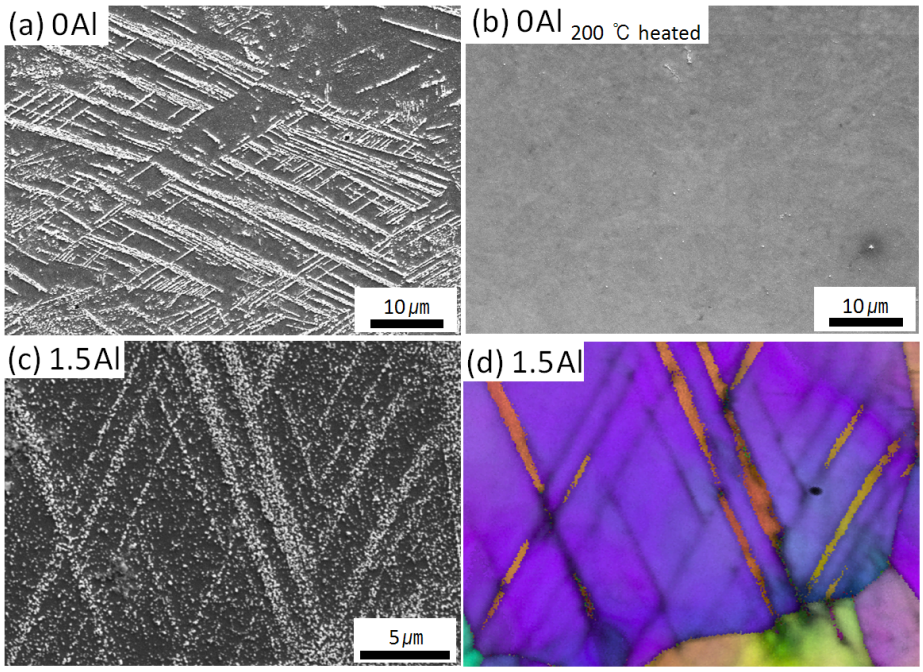

Figure 9. Images from hydrogen microprinting technique (HMT) in (a) 0Al, (c) 1.5Al alloys strained to 30%. (b) HMT image of (a) after heating to 200°C releasing most of diffusible hydrogen. (d) EBSD mapping for the same region of (c)

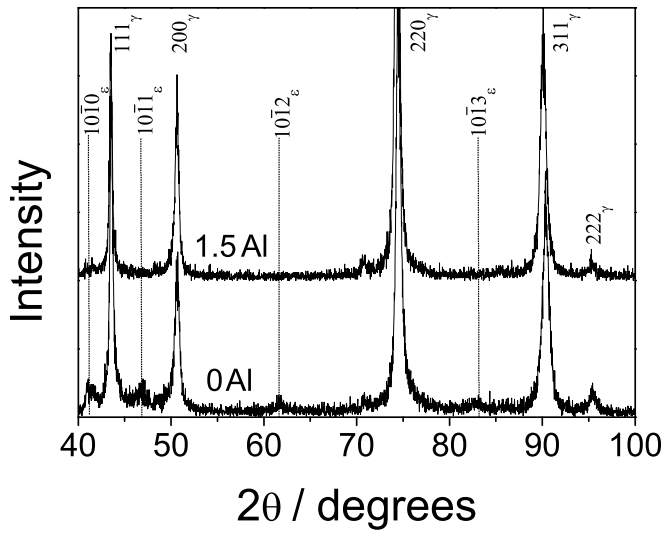

(a)

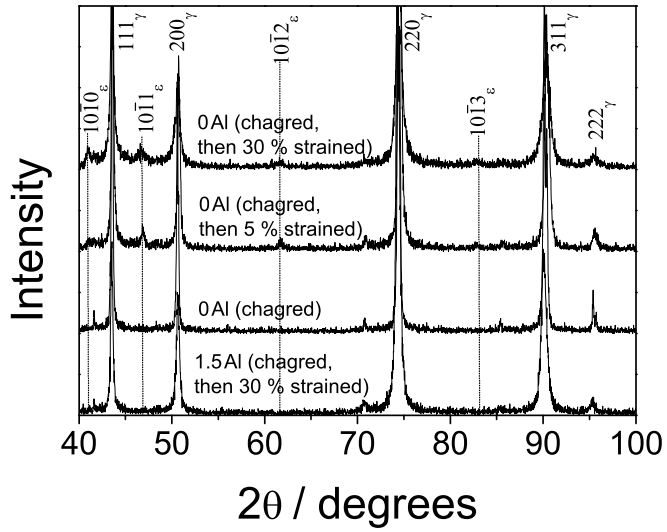

(b)

Figure 10. XRD profiles (a) from fractured samples by SSRT test with in-situ hydrogen charging and (b) from samples subjected to pre-charging followed by straining

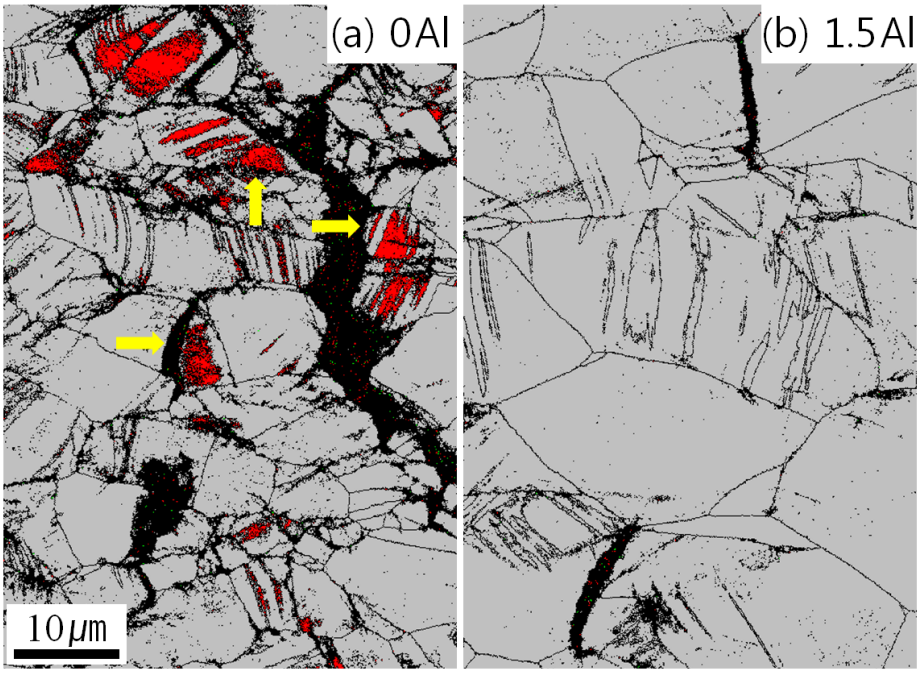

Figure 11. EBSD phase mapping (grey: austenite, red: ϵ–martensite, black: region with confidence index below 0.1) of (a) 0Al and (b) 1.5Al alloys subjected to pre-charging, strained to 30%

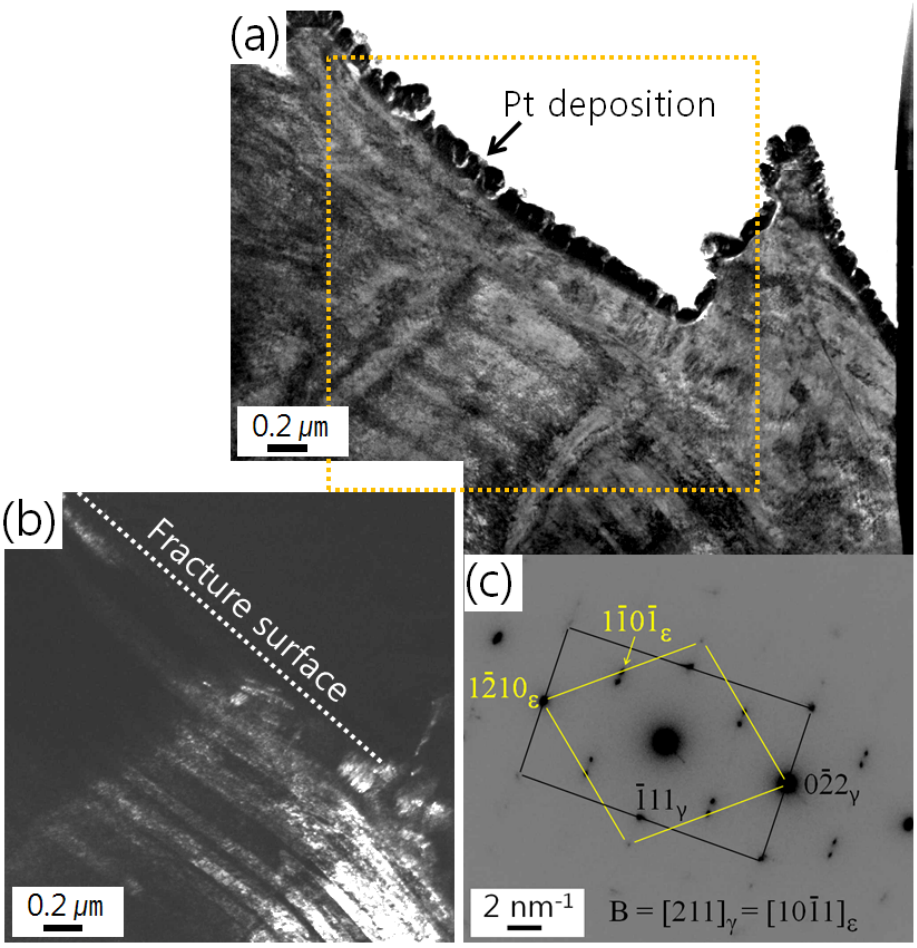

Figure 12. TEM micrographs of 0Al alloy subjected to SSRT test with in-situ hydrogen charging at 1 A m^{-2}. (a) BF image, (b) DF image of ϵ–martensite and (c) corresponding diffraction pattern

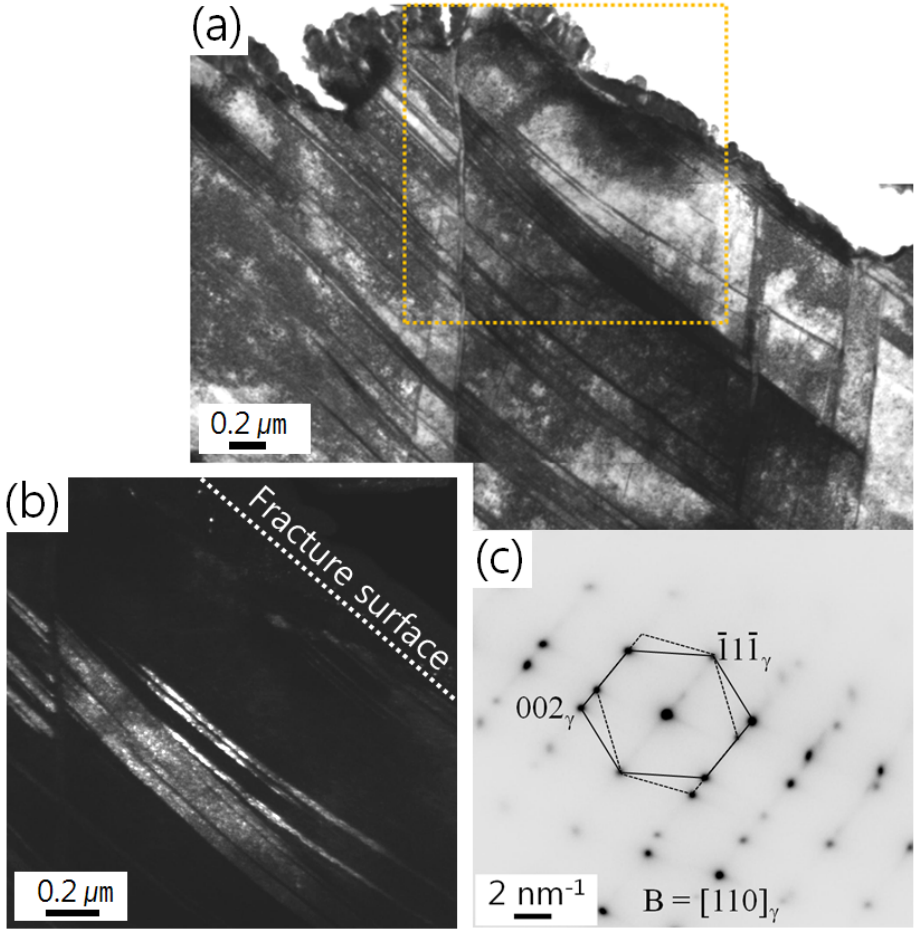

Figure 13. TEM micrographs of 1.5Al alloy subjected to SSRT test with in-situ hydrogen charging at 1 A m^{-2}. (a) BF image, (b) DF image of mechanical twin and (c) corresponding diffraction pattern